

Rotation and H α emission in a young SMC cluster: a spectroscopic view of NGC 330

PAUL I. CRISTOFARI ¹, ANDREA K. DUPREE ¹, ANTONINO P. MILONE ^{2,3}, MATTHEW G. WALKER ⁴,
MARIO MATEO ⁵, AARON DOTTER ⁶ AND JOHN I. BAILEY III ⁷

¹*Center for Astrophysics | Harvard & Smithsonian, 60 Garden Street, Cambridge, MA 02138, USA*

²*Dipartimento di Fisica e Astronomia “Galileo Galilei”, Univ. di Padova, Vicolo dell’Osservatorio 3, Padova, IT-35122*

³*Istituto Nazionale di Astrofisica - Osservatorio Astronomico di Padova, Vicolo dell’Osservatorio 5, Padova, IT-3512*

⁴*McWilliams Center for Cosmology, Carnegie Mellon University, 5000 Forbes Ave, Pittsburgh, PA 15213, USA*

⁵*Department of Astronomy, University of Michigan, Ann Arbor, MI 48109, USA*

⁶*Department of Physics and Astronomy, Dartmouth College, 6127 Wilder Laboratory, Hanover, NH 03755, USA*

⁷*California Institute of Technology - Caltech Optical Observatories, Pasadena, CA 91125, USA*

ABSTRACT

We present an analysis of high-resolution optical spectra recorded for 30 stars of the split extended main-sequence turnoff (eMSTO) of the young (~ 40 Myr) Small Magellanic Cloud (SMC) globular cluster NGC 330. Spectra were obtained with the M2FS and MIKE spectrographs located on the Magellan-Clay 6.5 m telescope. These spectra revealed the presence of Be stars, occupying primarily the cool side of the split main sequence (MS). Rotational velocity ($v \sin i$) measurements for most of the targets are consistent with the presence of two populations of stars in the cluster: one made up of rapidly rotating Be stars ($\langle v \sin i \rangle \approx 200 \text{ km s}^{-1}$), and the other consisting of warmer stars with slower rotation ($\langle v \sin i \rangle \approx 50 \text{ km s}^{-1}$). Core emission in the H δ photospheric lines was observed for most of the H α emitters. The shell parameter computed for the targets in our sample indicate that most of the observed stars should have inclinations below 75° . These results confirm the detection of Be stars obtained through photometry, but also reveal the presence of narrow H α and H δ features for some targets that cannot be detected with low-resolution spectroscopy or photometry. Asymmetry variability of H α line profiles on the timescales of a few years is also observed, and could provide information on the geometry of the decretion disks. Observations revealed the presence of nebular H α emission, strong enough in faint targets to compromise the extraction of spectra and to impact narrow band photometry used to assess the presence of H α emission.

1. INTRODUCTION

Over the last decades, high precision photometric measurements have provided evidence of an extended main sequence turnoff (eMSTO) and split main sequence (MS) in the color-magnitude diagrams (CMD) of intermediate-age (Milone et al. 2009) and young globular clusters (e.g., Milone et al. 2013, 2017; Correnti et al. 2017). The discovery of the eMSTO and split MS indicates the presence of multiple populations in globular clusters with possible variations in ages, metallicities, or rotation. Different scenarios have been offered to explain those observations, some proposing that multiple generations of stars formed in those clusters, or postu-

lating an extended star formation period on scales of a few 100 Myrs (Mackey et al. 2008; Milone et al. 2009; Conroy & Spergel 2011; Keller et al. 2011; Goudfrooij et al. 2014), others proposing that stellar rotation plays a major role in the appearance of multiple stellar populations (Bastian & de Mink 2009; D’Antona et al. 2017). None appear to account for all aspects of the observations (Bastian & Lardo 2018). The detailed characterization of stellar populations within globular clusters remains, therefore, essential to unveil the origin of the observed eMSTO and split MS.

Recent photometric and spectroscopic studies have suggested that the split MS likely results from two distinct populations of stars: one made up of B stars rotating close to the breakup velocity and surrounded by a decretion disk responsible for emission lines (Be stars), the other composed of hotter B stars with slower rotation (D’Antona et al. 2015; Milone et al. 2016; Bastian

et al. 2017; Dupree et al. 2017). The presence of fast-rotating Be stars was confirmed by the detection of H α emission, believed to be directly linked to the presence of Be stars (Rivinius et al. 2013), via high-resolution spectroscopic measurements in NGC 1866 (Dupree et al. 2017). Those results further suggested that a difference in rotation velocities should be observed between the two populations within a same cluster, although the rotation velocities of Be stars could not be estimated from H α emission lines.

The current work focuses on the young cluster NGC 330 of the Small Magellanic Cloud (SMC) whose age was reported to be between 30 and 45 Myr (Keller et al. 2000; Milone et al. 2018; Eldridge et al. 2020; Patrick et al. 2020), and metallicity is expected to be $[\text{Fe}/\text{H}] \lesssim -1.0$ dex (e.g., Piatti et al. 2019). Previous photometric studies of the cluster have reported a large number of Be stars (Milone et al. 2018), consistent with the works of Wisniewski & Bjorkman (2006). Iqbal & Keller (2013) proposed that a low-metallicity environment may produce a relatively large fraction of Be stars. A study of the multiplicity of NGC 330 from low-resolution spectra ($R < 4000$, Bodensteiner et al. 2021) reported binary fractions in different regions of the color magnitude diagram (CMD), finding in particular a binary fraction of 6% within the Be stellar population. Such results provide additional constraints for the previously mentioned scenarios. A recent study published rotational velocity estimates for B and Be stars in NGC 330 obtained from low-resolution ($R < 4000$) MUSE spectra (Bodensteiner et al. 2023). The work presented here focuses on stars observed in the same cluster, but relies on high-resolution ($R > 25000$) spectra, permitting us to probe the profiles of the observed spectral lines.

In this paper, we present the results of a study of high resolution spectra recorded for dozens of targets in NGC 330. We targeted the H α line in order to assess the presence of emission features, and a He I line at 4143.76 Å in order to estimate the rotational velocity of the targets. The spectroscopic material and reduction of the data are introduced in Sec. 2 and the results are presented in Sec. 3. Those results are then discussed in Sec. 4.

2. OBSERVATIONS AND DATA REDUCTION

Target coordinates and Hubble Space Telescope (HST) magnitudes were extracted from Milone et al. (2018) and listed in Tables 1 & 2. Targets observed with the Michigan/Magellan Fiber System (M2FS, Mateo et al. 2012) were selected so that no other star was found within 2'' of a target, unless the magnitude of the second star was fainter, with a magnitude differ-

ence between the two stars in the F814W filter larger than 1.8. Targets observed with the Magellan Inamori Kyocera Echelle (MIKE, Bernstein et al. 2003) were selected among the brightest known stars in the cluster. Targets 58, 68, 73, 75 and 100 were observed both with M2FS and MIKE.

MIKE spectra were recorded between November 27 to 29, 2021, with the blue and red arms, covering 3350–9500 Å. For each target, 2 to 4 exposures of 1200 to 1800 s were obtained and summed in order to obtain the final spectra.

With M2FS, spectra were recorded in 2019 and 2022. Observations were carried out with two filters: a Li-H α filter, and a so-called ‘Dupree-blue’ filter. The Li-H α filter allows us to capture two orders in the 6530–6790 Å wavelength range for up to 128 targets at once. The Dupree-blue filter, specifically built to target He I lines and never used before this study, was designed to cover 3970–4196 Å over 4 orders, allowing spectra of up to 64 targets to be recorded simultaneously.

Table 3 summarizes the exposure times and number of exposures for each observation night. All spectra recorded with MIKE and M2FS were doppler shifted to the rest frame assuming a bulk velocity of 180 km s $^{-1}$ for NGC 330. The resolving powers of MIKE and M2FS are similar for the considered modes and wavelength ranges ($R \approx 25000$ and $R \approx 30000$, respectively).

2.1. M2FS data reduction

Data were reduced through a Python pipeline largely described in Walker et al. (2023), and adapted to meet our needs¹ (Cristofari & Walker 2024). In this section, we briefly describe the main steps of the reduction. Raw data consists of images obtained through 4 amplifiers for each of the two detectors. Bias, overscan and dark corrections are applied independently for each amplifier, relying on the Python `astropy/ccdproc` package (Craig et al. 2017). For each detector, the 4 images are then joined to generate the full frames used to extract the spectra. Aperture traces were identified on flat images, and used to extract the spectra from science frames. Wavelength calibration was performed by identifying known lines from ThAr exposures obtained right before or between two science exposures.

The extracted spectra contain emission sky lines. Several M2FS fibres pointing to the sky were used to extract sky spectra that were combined in order to obtain a template sky spectrum (see Fig. 1). For each science spectrum, the intensity of the sky template was adjusted

¹ <https://github.com/pcristof/M2FS-RS>

Table 1. Targets observed with M2FS and their parameters.

Target	R.A. (2000.0) [hh:mm:ss]	Decl. (2000.0) [dd:mm:ss]	m_{F814W}^a	m_{F336W}^a	Color ^b	H α excess ^c	H α ^d	$v \sin i^e$	shell ^f
2	14.067688 [00:56:16.25]	-72.461457 [-72:27:41.24]	16.412	15.391	-1.020	-0.724	e	296	1.2
3	14.082867 [00:56:19.89]	-72.460028 [-72:27:36.10]	15.417	14.118	-1.299	-1.692	e	185	...
5	14.066931 [00:56:16.06]	-72.466429 [-72:27:59.15]	16.071	14.757	-1.314	-1.844	e	203	...
7	14.095990 [00:56:23.04]	-72.465020 [-72:27:54.07]	15.133	13.924	-1.210	-1.665	e	98	1.1
18	14.051482 [00:56:12.36]	-72.463192 [-72:27:47.49]	17.335	16.332	-1.002	-1.695	e	...	1.7
33	14.107634 [00:56:25.83]	-72.458606 [-72:27:30.98]	17.097	16.038	-1.059	-1.643	e	398	1.1
58	14.059443 [00:56:14.27]	-72.475078 [-72:28:30.28]	15.726	14.689	-1.037	-2.085	e	292	...
61	14.043880 [00:56:10.53]	-72.454236 [-72:27:15.25]	17.138	15.658	-1.480	-0.327	e
64	14.070223 [00:56:16.85]	-72.449696 [-72:26:58.91]	17.430	16.395	-1.035	-0.965	e	...	>2.0
68	14.106100 [00:56:25.46]	-72.451997 [-72:27:07.19]	15.366	14.213	-1.152	-1.727	e	55	1.4
73	14.027701 [00:56:06.65]	-72.460096 [-72:27:36.35]	14.389	13.079	-1.309	-1.568	e	168	...
75	14.129855 [00:56:31.17]	-72.466128 [-72:27:58.06]	15.402	14.310	-1.092	-1.794	e	246	...
76	14.049814 [00:56:11.96]	-72.477142 [-72:28:37.71]	17.319	16.113	-1.206	-0.913	e	...	1.4
94	14.125068 [00:56:30.02]	-72.450499 [-72:27:01.80]	17.603	16.579	-1.024	-0.185	e
95	14.048756 [00:56:11.70]	-72.480595 [-72:28:50.14]	17.921	16.989	-0.931	-1.161	e
98	14.019112 [00:56:04.59]	-72.453643 [-72:27:13.11]	17.847	16.930	-0.917	-0.201	e
109	14.141323 [00:56:33.92]	-72.478912 [-72:28:44.08]	18.038	17.221	-0.817	-0.823	e	117	...
47	14.042005 [00:56:10.08]	-72.459053 [-72:27:32.59]	14.481	13.178	-1.303	-0.436	a	45	...
49	14.044407 [00:56:10.66]	-72.469560 [-72:28:10.42]	15.184	13.678	-1.507	...	a	47	...
53	14.039188 [00:56:09.41]	-72.466356 [-72:27:58.88]	14.452	13.199	-1.253	-0.432	a	49	...
66	14.073804 [00:56:17.71]	-72.477194 [-72:28:37.90]	16.594	15.132	-1.462	-0.284	a
97	14.028371 [00:56:06.81]	-72.476448 [-72:28:35.21]	15.942	14.163	-1.779	...	a	109	...
100	14.099138 [00:56:23.79]	-72.483452 [-72:29:00.43]	16.358	14.960	-1.398	-0.315	a

^aHST magnitudes from Milone et al. (2018).

^bColor defined as $m_{F336W} - m_{F814W}$.

^cH α excess defined as $m_{F656N} - m_{F814W}$.

^dH α line shape (emission e, or absorption a).

^e $v \sin i$ in km s^{-1} derived by fitting TLUSTY models to the He I line at 4143.76 Å and the H δ line. A 50 km s^{-1} uncertainty on $v \sin i$ was estimated for our method.

^fShell parameter defined as the ratio between the average of the blue and red maxima of the H α line and the center of the H α line.

in order to remove the sky emission features. Although this approach efficiently removes OH lines, residual H α emission is visible in the sky spectra and cannot be fully corrected this way (see Sec. 3.1).

2.2. MIKE data reduction

MIKE data were reduced with the Carnegie Python Distribution (CarPy) developed by D. Kelson (Kelson et al. 2000; Kelson 2003). CarPy was used to perform aperture extraction, wavelength calibration, and to normalize the extracted orders. One of the advantages of MIKE over M2FS, as will become clear in Sec. 3.1, is the possibility to extract the sky and science spectra

from each aperture (see Fig. 2), producing accurate sky subtractions (Kelson 2003).

2.3. Spectral features selection

H α and He I lines were the targets of this study in order to assess the presence of Be stars and estimate their projected rotational velocities. With M2FS, the H α line and a He I line at 4143.76 Å were extracted from the two filters. With MIKE, several Hydrogen lines from the Balmer series and up to 13 Helium lines were extracted. Extracted spectra were normalized with a low degree polynomial in the region surrounding those lines.

3. RESULTS

Table 2. Targets observed with MIKE and their parameters.

Target	R.A. (2000.0) [hh:mm:ss]	Decl. (2000.0) [dd:mm:ss]	m_{F814W}^a	m_{F336W}^a	Color ^b	H α excess ^c	H α ^d	$v \sin i^e$	shell ^f
52	14.050572 [00:56:12.14]	-72.454745 [-72:27:17.08]	15.232	14.003	-1.229	-1.419	e	161	...
56	14.073880 [00:56:17.73]	-72.475708 [-72:28:32.55]	15.509	14.373	-1.135	-1.611	e	220	...
58	14.059443 [00:56:14.27]	-72.475078 [-72:28:30.28]	15.726	14.689	-1.037	-2.085	e	270	...
68	14.106100 [00:56:25.46]	-72.451997 [-72:27:07.19]	15.366	14.213	-1.152	-1.727	e	55	1.2
73	14.027701 [00:56:06.65]	-72.460096 [-72:27:36.35]	14.389	13.079	-1.309	-1.568	e	209	...
75	14.129855 [00:56:31.17]	-72.466128 [-72:27:58.06]	15.402	14.310	-1.092	-1.794	e	259	...
83	14.062130 [00:56:14.91]	-72.479919 [-72:28:47.71]	15.245	14.274	-0.971	-1.960	e	261	1.2
84	14.134507 [00:56:32.28]	-72.463979 [-72:27:50.32]	15.344	14.092	-1.253	-1.309	e	115	...
51	14.113468 [00:56:27.23]	-72.458694 [-72:27:31.30]	16.310	15.011	-1.299	-0.303	a	24	...
69	14.060394 [00:56:14.49]	-72.476796 [-72:28:36.47]	16.370	14.967	-1.402	-0.322	a	48	...
88	14.128804 [00:56:30.91]	-72.472024 [-72:28:19.29]	15.728	14.271	-1.457	-0.333	a	34	...
100	14.099138 [00:56:23.79]	-72.483452 [-72:29:00.43]	16.358	14.960	-1.398	-0.315	a	67	...

^aHST magnitudes from Milone et al. (2018).

^bColor defined as $m_{F336W} - m_{F814W}$.

^cH α excess defined as $m_{F656N} - m_{F814W}$.

^dH α line shape (emission e, or absorption a).

^e $v \sin i$ in km s^{-1} derived by fitting TLUSTY models to five He I lines at 4009.27, 4026.191, 4120.82, 4143.76 and 4387.929 Å. A 50 km s^{-1} uncertainty on $v \sin i$ was estimated for our method.

^fShell parameter defined as the ratio between the average of the blue and red maxima of the H α line and the center of the H α line.

Table 3. Observations used in this work.

Date	Filter ^a	No. exp.	Exp. time (s)	Instrument	Total time (hrs)
2019 Nov. 16	Li-H α	4	2100	M2FS	2.3
2022 Sep. 20	Li-H α	4	1800	M2FS	2.0
2022 Sep. 21	Dupree-blue	6	1800	M2FS	3
2021 Nov. 27 – 29	...	2 – 4	1200 – 1800	MIKE	0.7 – 2.0

^aThe wavelength coverage of the M2FS filters are 6540–6790 Å for the Li-H α filter, and 3970–4196 Å for the Dupree-blue filter. MIKE spectra cover the 3350–9500 Å wavelength range.

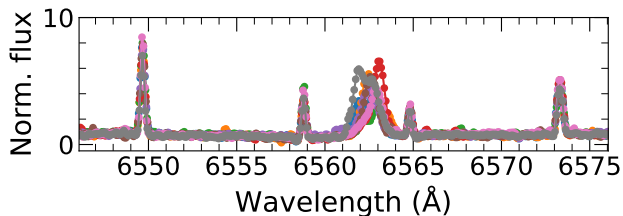


Figure 1. Normalized sky spectra recorded with M2FS. The sharp, thin emission lines are OH lines, while the central line is H α emission originating from the nebula. The colors correspond to spectra extracted from different sky apertures.

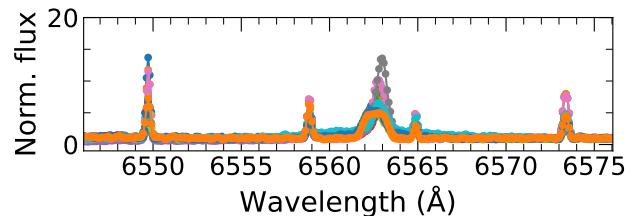


Figure 2. Same as Fig. 1 for the skies recorded with MIKE. The colors correspond to different sky spectra extracted from the apertures.

M2FS and MIKE high-resolution spectra are used to identify and characterize the H α line, that was visually

inspected for all targets, in order to search for emission and or/absorption features, providing information on the presence of a decretion disk around B stars (Riv-

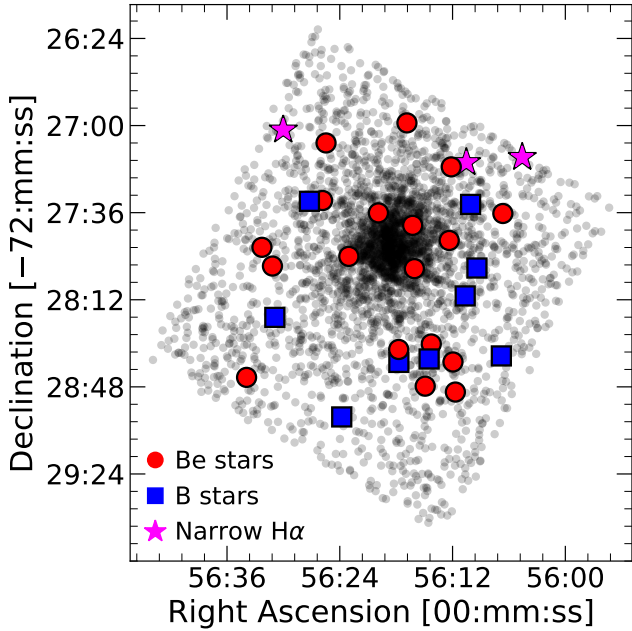


Figure 3. Position of the stars on the sky. Declinations are given in degrees, arc minutes and arc seconds, while right ascensions are in hours, minutes and seconds. Gray circles mark the position of 2827 targets in the direction of NGC 330 (Milone et al. 2018). We mark the position of the identified Be stars (red circles), and B stars (blue squares), and the three narrow H α emitters (fuchsia stars).

inius et al. 2013). Because H α emission lines do not provide direct information on the rotational velocity of the identified Be stars (Dupree et al. 2017), fits of synthetic spectra were performed on He I lines to estimate the projected rotational velocity ($v \sin i$) of the targets.

3.1. Nebular emission in NGC 330

Inspection of the spectra recorded with M2FS and MIKE revealed a broad emission feature in the fibers pointing at the sky (see Figs. 1 & 2). The shape and intensity of this feature strongly vary among fibers and apertures, and are caused by nebular emission. With M2FS, sky spectra were not recorded immediately next to each target, but in dedicated fibers pointing in the direction of the nebula. Consequently, accurately removing the nebular features is not possible. Instead, we rely on the OH lines to fit a sky template spectrum and remove an averaged nebular emission feature. Because this correction can be sub-optimal, spectra were inspected both with and without sky subtraction in order to assess the impact of the nebular features on the shape of the stellar H α line. The nebular emission significantly contributes to the spectra of faint targets, making it difficult to draw conclusion regarding the core of the stellar H α line. Nebular emission was reported in

previous studies of stars in NGC 330 (e.g., Bodensteiner et al. 2023). Low-resolution spectroscopy is unlikely to clearly resolve the narrow emission line coming from the nebula.

3.2. Hydrogen emission features

Out of the 30 targets observed with M2FS and/or MIKE (see Fig. 3), H α emission features were detected for 21 of them (assumed to indicate the presence of Be stars), and H α broad absorption lines were observed for 9 of them (see Fig. A1). Three of those targets have strong but narrower H α emission lines.

The shape of the H α line is expected to provide information on the inclination the targets (Rivinius et al. 2013; Sigut & Ghafourian 2023). For some targets, such as objects 75 and 58, the ‘wine-bottle’ shape of the H α line is typically associated with low inclination angles (with a star viewed almost pole-on). Other targets (e.g., 18, 64, 68, 83) show signs of deep core reversal with various depths, expected for stars viewed with different inclination angles (Rivinius et al. 2013; Sigut & Ghafourian 2023). The inaccurately corrected nebular emission in the M2FS spectra renders the precise study of the H α line core difficult for some targets. Previous studies (Hanuschik 1996; Sigut & Ghafourian 2023) have reported a link between the shell parameter (i.e. the ratio between the average of the maxima on each side of the H α line center and the H α line center) and the inclination of the star. In particular, Sigut & Ghafourian (2023) found that shell parameters above 1.5 tend to indicate inclinations above 75°. Shell parameters derived from the M2FS and MIKE spectra are reported in Tables 1 and 2, and were found to be above 1.5 for only 2 targets (18 and 64) suggesting that most of the other stars in our sample have inclinations below 75° (here, $i = 0^\circ$ corresponds to a star seen pole-on and $i = 90^\circ$ implies that the rotation axis is perpendicular to the line of sight). Large asymmetries were observed in the H α lines for several targets (e.g. targets 7, 64, 68, 73, 95). We note that if the observed targets were interacting binaries, the complexity of the circumstellar disk is expected to impact the shape of the H α line (Zorec et al. 2023).

The photometric data acquired through the Hubble F656N H α filter (see Fig. 4) reveal excesses consistent with the identified broad H α emission features. Among the stars for which H α emission was detected, a few of them (e.g. objects 2, 76, 95, 109, see Fig. A1) show significantly shallower emission than others, and correspond to the stars whose excess in the H α filter ($m_{F656N} - m_{F814W}$) are found between -0.5 and -1.0 (see Fig. 4).

Emission in other Hydrogen lines from the Balmer series is expected to originate from regions closer to the central star than $H\alpha$ lines. For several Be stars, $H\delta$ emission features were observed at the center of $H\delta$ photospheric absorption. The $H\delta$ emission appears sharp for several targets whose $v \sin i$ are lower than 100 km s^{-1} (see Sec. 3.5). Narrow deep absorption features are also observed at the center for the $H\delta$ line for targets 64 and 18 that have deep $H\alpha$ core reversal, and for target 83, which could result from absorption caused by the decretion disk at large inclination angles. Such emission features are also observed in the spectra recorded with MIKE for several hydrogen lines of the Balmer series; in particular for target 68 and 84 (see Fig. A2).

The analysis of the MIKE spectra revealed additional features, including up to 8 Fe II emission lines (see Table 4). For targets 58, 68, 73, 83 and 84, two of those Fe II emission lines appear on the red side of the helium lines at 4922 \AA and 5015 \AA , leading to line shapes that resemble a P Cygni profile. For several of those targets, the cores of the helium lines at 5875 , 6678 and 7065 \AA are also shallower than predicted by the models, often asymmetric, or reveal helium emission lines. Those features could indicate the presence of winds.

3.3. Narrow $H\alpha$ emitters

The spectra of a few targets, such as 61, 94 or 98, display intense and narrow $H\alpha$ emission lines, whose interpretation is limited by the presence of nebular emission (see Fig. A1). Clear photospheric $H\delta$ absorption lines are observed for the three targets, and a narrow emission feature is visible at the center of these absorption lines. We refer to those three targets as ‘narrow $H\alpha$ emitters’ in the rest of the paper.

The full width at half maximum (FWHM) of the $H\delta$ and $H\alpha$ emission features are on the order of $\sim 50 \text{ km s}^{-1}$ for the three narrow $H\alpha$ emitters, while the equivalent widths of the emission component of the $H\alpha$ lines are significantly larger than that of $H\delta$ lines. This is consistent with the spectra expected for Be stars, with $H\delta$ lines originating from regions in the disk closer to the central star and hence weaker. Larger equivalent widths for $H\alpha$ lines than for other hydrogen lines are found for all Be stars in our sample.

3.4. Temporal evolution of $H\alpha$ profiles

The spectra recorded with M2FS in 2019 and 2022, and with MIKE in 2021 reveal variations of the $H\alpha$ emission line shape (see Fig. 6). For some targets, such as 2, 18 or 75, variations in the strength of the emission lines are observed. For other targets, such as 64 or 68, changes in the asymmetry of the line shapes are visible.

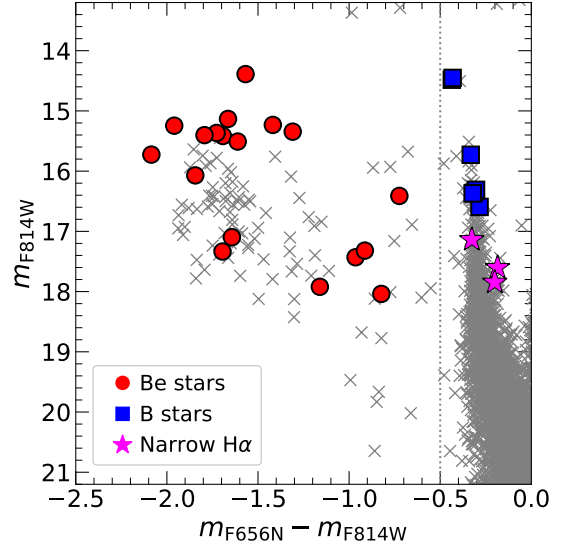


Figure 4. Comparison between the F814W magnitude and relative excess in the $H\alpha$ F656N filter. Gray crosses mark the position of 2827 stars in NGC330 (Milone et al. 2018). Red circles and blue squares mark the position of Be stars and B stars, respectively. Fuchsia stars mark the position of 3 ‘narrow $H\alpha$ emitters’ for which narrow $H\alpha$ and $H\delta$ emission lines were observed. The dashed gray line shows the fiducial boundary at $m_{F656N} - m_{F814W} = -0.5$ separating the population of $H\alpha$ emitters and absorbers from HST photometry (Milone et al. 2018).

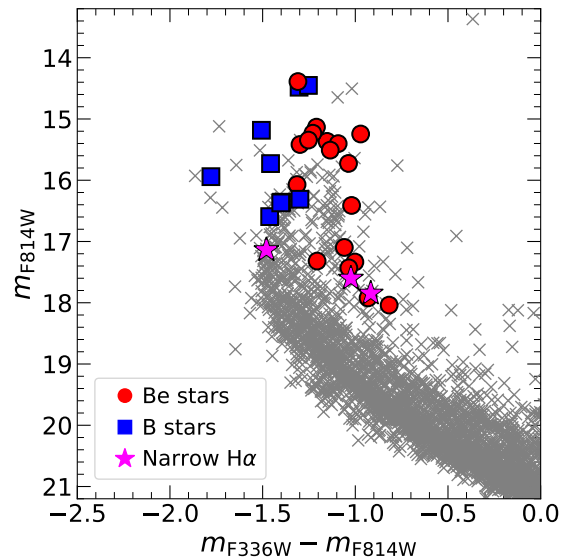


Figure 5. Color-magnitude diagram for NGC330 targets. Gray crosses mark the position of 2827 stars in NGC330 (Milone et al. 2018). Red circles and blue squares mark the position of Be stars and B stars, respectively. Fuchsia stars mark the position of the 3 ‘narrow $H\alpha$ emitters’ for which narrow $H\alpha$ and $H\delta$ emission lines were observed.

Table 4. He I and Fe II lines identified in the MIKE spectra.

Wavelength (Å)	Species	Ref. ^a
3634.23	He I	NIST
3634.24	He I	NIST
3651.99	He I	NIST
3705.01	He I	NIST
3819.79	He I	NIST
3867.48	He I	NIST
3871.79	He I	NIST
3964.73	He I	NIST
4009.27	He I	NIST
4026.19	He I	NIST
4120.82	He I	NIST
4143.76	He I	NIST
4169.18	He I	NIST
4387.93	He I	NIST
4437.55	He I	NIST
4471.48	He I	NIST
4713.31	He I	NIST
4921.93	He I	NIST
5015.68	He I	NIST
5047.74	He I	NIST
5875.61	He I	NIST
6678.15	He I	NIST
7065.18	He I	NIST
4549.20	Fe II	NIST
4923.92	Fe II	NIST
5018.44	Fe II	NIST
5169.03	Fe II	NIST
5316.61	Fe II	NIST
6318.12	Fe II	K13
6347.55	Fe II	NIST
6371.72	Fe II	NIST

^aReference used for the identification of the spectral line. NIST: NIST database version 5.11 (Kramida et al. 2023). K13: R. Kurucz calculations, 2013, available at <http://kurucz.harvard.edu/atoms/2601/gfemq2601.pos> and accessed through the VALD database.

For target 64, the H α line exhibits two main peaks, with the blue side of the line being more intense than the red side in 2019. In 2022 the asymmetry is reversed: the red side is stronger than the blue side. A somewhat similar evolution is observed for target 68 between 2019 and 2021/2022.

The evolution of the H α line shape tracks movement in the emitting regions of the decretion disk. Variations in the strength of the H α line, in particular, have been proposed to arise from fluctuations in the extent of the emission region (Vinicius et al. 2006). Slowly revolving

perturbation patterns, sometimes referred to as ‘one-armed’ oscillations (Okazaki 1991, 1997; Papaloizou & Savonije 2006), have been proposed to explain asymmetric hydrogen line profiles and their evolution, in which excess emission in the blue or red side of a spectral line is attributed to enhanced temperature and density in the approaching or receding side of the disk. This is further supported by the observation of similar asymmetries in the H β , H γ , and H δ lines recorded with MIKE for targets 52, 68, 73 and 84 (see Figs. B3).

3.5. Rotational velocities

Because the rotational velocities of the targeted stars are expected to be large, we assumed that rotation is the main source of broadening in the spectra. Following the results of Bodensteiner et al. (2023), we derived $v \sin i$ measurements by fitting synthetic models taken from the TLUSTY BSTAR2006 grid (Hubeny & Lanz 1995; Lanz & Hubeny 2007) to the spectra. For spectra recorded with M2FS, the fit is performed on the He I line at 4143.76 Å and the H δ line making sure to ignore the central emission feature. For spectra recorded with MIKE, we rely on 5 of the best modeled He I lines at 4009.27, 4026.191, 4120.82, 4143.76 and 4387.929 Å, allowing us to improve the fits to the data.

For each spectrum, a least-squares fit is performed to obtain the best fitting TLUSTY model. Specifically, rotational velocity is included in the model by convolving the synthetic spectra with a rotation profile. A fit is obtained for each combination of effective temperature (T_{eff}) and log surface gravity ($\log g$) assuming a metallicity $Z = 0.1 Z_{\odot}$ (Piatti et al. 2019), leading to computation of a grid of χ^2 values and associated $v \sin i$. The fit leading to the lowest χ^2 is then considered the best match, and used to obtain $v \sin i$. This approach provides a very rough estimate of T_{eff} and $\log g$, given that the fit is obtained from a limited number of spectral features. Several tests have allowed us to confirm that varying T_{eff} by up a few thousands of kelvins or $\log g$ by 0.5 dex had limited impact on the modeled line shape and the derived $v \sin i$, with typical differences of less than 50 km s^{-1} . This impact is, however, larger than the formal uncertainties computed from the spectral fit. Given the degeneracy and the large uncertainties on the atmospheric parameters, conservative error bars of $\pm 50 \text{ km s}^{-1}$ on the $v \sin i$ measurements were adopted, to account for some of the systematic errors of the method.

For targets identified as B stars, our values of $v \sin i$ range from about 30 to 100 km s^{-1} . Although this contrasts with previous results suggesting a larger range of rotational velocities for B stars in the cluster (Boden-

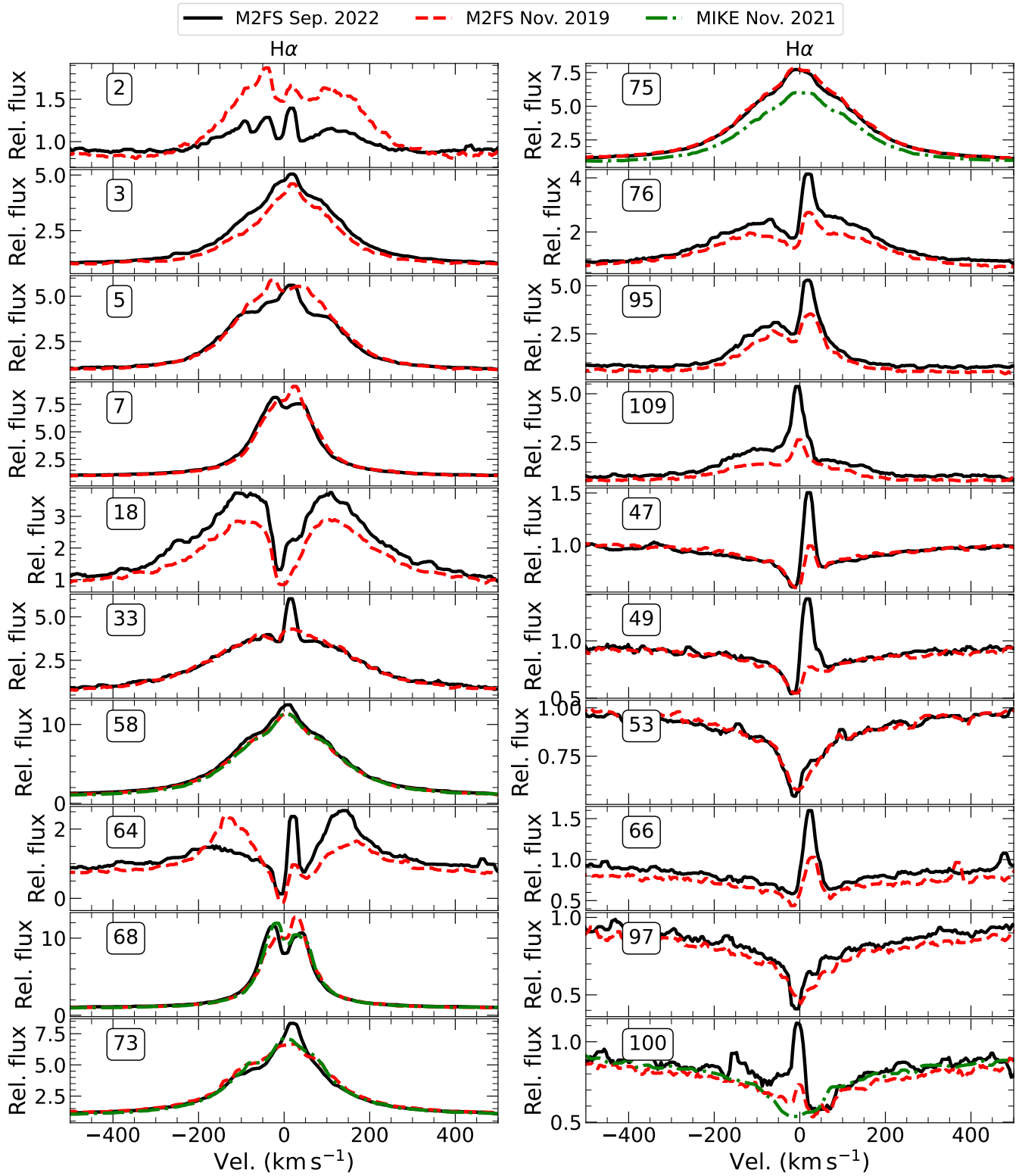


Figure 6. Comparison between sky-corrected spectra recorded in 2019 (red broken line) and 2022 (solid black line) with M2FS, and in 2021 with MIKE (dotted-dashed green line).

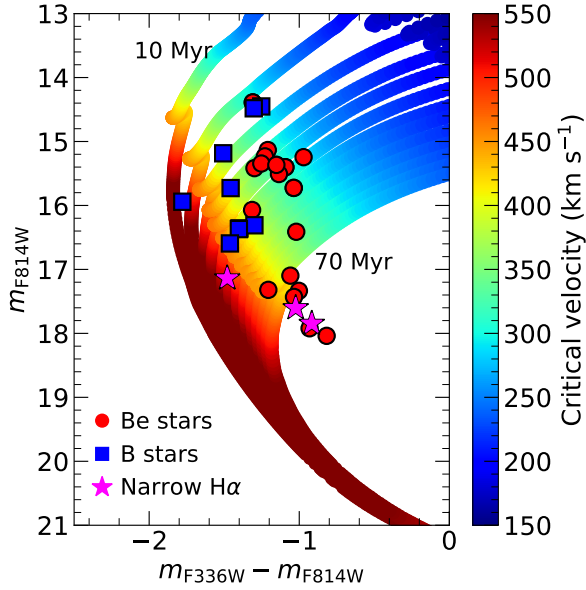


Figure 7. Breakup velocities for MIST isochrones with ages ranging from 10 to 70 Myr and $[\text{Fe}/\text{H}] = -0.85$ dex. Red circles and blue squares mark the position of Be stars and B stars, respectively. Fuchsia stars mark the position of the 3 ‘narrow $\text{H}\alpha$ emitters’ for which narrow $\text{H}\alpha$ and $\text{H}\delta$ emission lines were observed.

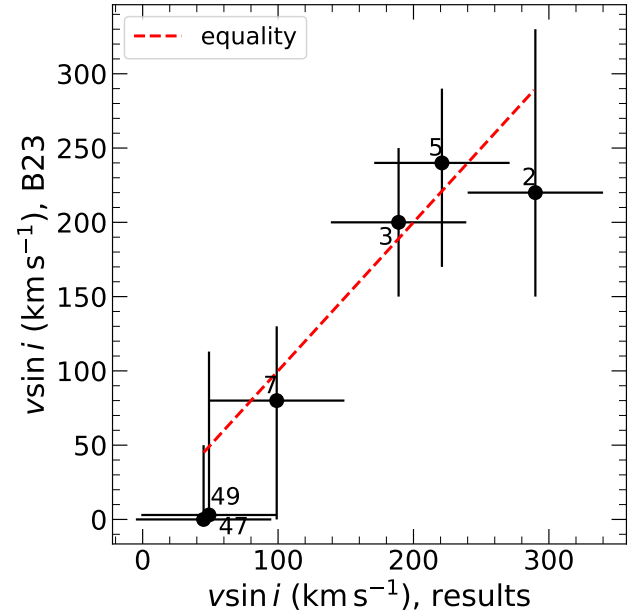


Figure 9. Comparison between the derived $v \sin i$ values and those of Bodensteiner et al. (2023, B23) for the 6 targets common to both studies. The red broken line marks the equality.

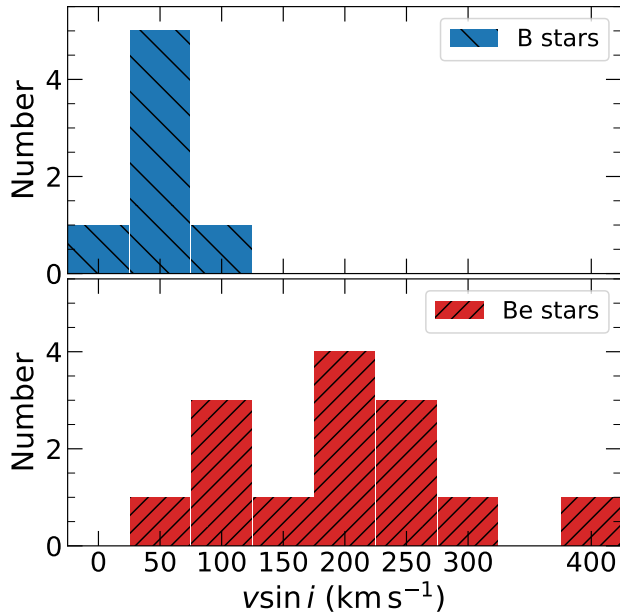


Figure 8. Distribution of the rotation velocities for the targets in our sample.

steiner et al. 2023), our targets are in the turnoff region of the CMD, and our results are consistent with the lower $v \sin i$ found by Bodensteiner et al. (2023) in this part of the diagram.

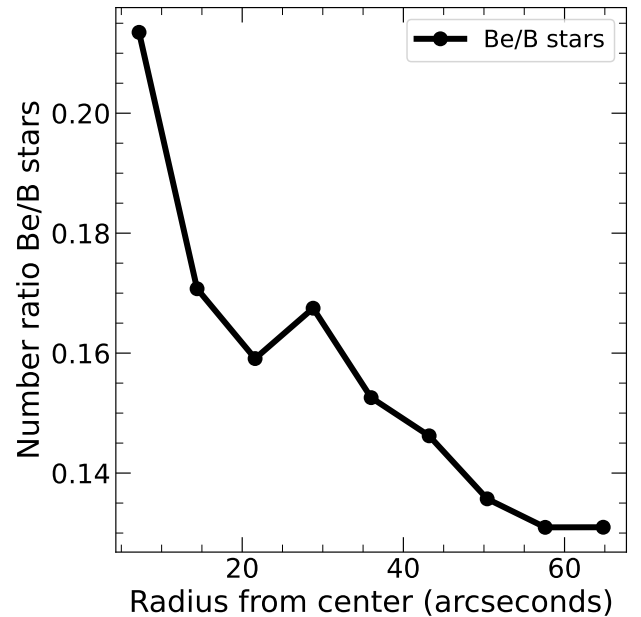


Figure 10. Number ratio of $N_{\text{Be}}/N_{\text{B}}$, with N_{Be} and N_{B} the number of Be and B stars found within a given radius from the cluster center, respectively. B and Be stars numbers were estimated from excess in the F656N HST filter (Milone et al. 2018).

For $H\alpha$ emitters, however, our $v \sin i$ estimates span a wide range values from ~ 50 to $\sim 400 \text{ km s}^{-1}$. We note that the 3 targets 7, 68 and 84 are the only stars with broad $H\alpha$ emission lines in our sample with $v \sin i < 100 \text{ km s}^{-1}$. The $v \sin i$ estimates obtained for most stars in our sample are consistent with the theoretical critical velocities computed with the MIST models (Paxton et al. 2011, 2013, 2015; Choi et al. 2016; Dotter 2016) for ages ranging between 10 to 70 Myr and a metallicity $[\text{Fe}/\text{H}] = -0.85$ dex (see Fig. 7). Those models predict critical velocities around 300 and 400 km s^{-1} for most of the Be stars in our sample.

The distribution of $v \sin i$ Be stars is centered on $\sim 200 \text{ km s}^{-1}$ (see Fig. 8). Assuming no selection bias, the distribution is consistent with a range of rotational velocities within the sample of Be stars, given that a random distribution of inclinations would favor high $\sin i$ values. The shell parameters obtained for the sample of stars, however, suggest that most of the targets have inclinations below 75° .

Five stars were observed both with M2FS and MIKE: targets 58, 68, 73, 75 and 100. For target 68, the $v \sin i$ estimates derived from M2FS and MIKE spectra differ by less than 1 km s^{-1} . For targets 58, 73 and 75, the estimates agree within $\sim 40 \text{ km s}^{-1}$, less than our estimated error bar of 50 km s^{-1} . The spectra recorded with M2FS for target 100 did not allow us to derive an estimate of $v \sin i$. A comparison between the obtained $v \sin i$ and those reported by Bodensteiner et al. (2023) is shown in Fig. 9. For the 6 targets included in both studies, the estimates agree within the error bars. The distribution of $v \sin i$ estimates obtained in this study are presented in Fig. 8, while the values are reported in Tables 1 and 2.

4. DISCUSSION AND CONCLUSIONS

Most of the $H\alpha$ emitters, assumed to be Be stars, are found in the red side of the split eMSTO, while the other targets fall within the blue branch of the split eMSTO. Those results confirm the detection of Be stars from photometric measurements (Milone et al. 2018) suggesting that the red branch of the split eMSTO is populated in the vast majority by Be stars. A clear difference is found between the average $v \sin i$ of the Be stellar population ($\langle v \sin i \rangle \approx 200 \text{ km s}^{-1}$) and that made up of stars with no $H\alpha$ emission ($\langle v \sin i \rangle \approx 50 \text{ km s}^{-1}$). The $v \sin i$ estimates are consistent with the expected critical velocities computed from MIST models, predicting breakup velocities around $300\text{-}400 \text{ km s}^{-1}$ for the Be stars in our sample. The results also confirm the previous measurements derived from low-resolution data (Bodensteiner et al. 2023), with excellent agreement between the obtained $v \sin i$ for the 6 targets common to both samples.

Computed shell parameters suggest that most stars in the sample have inclinations below 75° , effectively leading to an unexpectedly low number of high-inclination stars. It should be noted, however, that Sigut & Ghafourian (2023) also reports larger inclinations and shell parameters below 1.5 for some stars they have analyzed. Our $v \sin i$ estimates suggest, nonetheless, a range of rotational velocities in the population of Be stars. This is further supported by the observed $H\alpha$ line shapes, with several targets showing no clear sign of core reversal or asymmetry, in spite of large $v \sin i$ estimates (e.g. targets 58, 75), while the ‘wine-bottle’ shape of the lines is believed to arise from targets seen at low inclinations (Rivinius et al. 2013).

The observation of $H\delta$ emission features supports the presence of a decretion disk. $H\delta$ emission is expected to originate from regions closer to the central star (Klement et al. 2017; Zorec et al. 2023), and are not typical signatures of nebular emission (as confirmed by their absence from sky spectra). Two peculiar cases stand out in our data. First, for the three narrow $H\alpha$ emitters, $H\delta$ emission features were observed (targets, 61, 94, 98, see Fig. A1). Although part of the $H\alpha$ emission can originate from the nebula, the presence of photospheric $H\delta$ absorption lines, and narrow $H\delta$ emission in their core, suggest the presence of a Be star. No $H\alpha$ excess is detected in the Hubble F656N $H\alpha$ filter for those targets, most likely because of the narrow width of the observed lines. Thus, those targets could easily be inaccurately classified from HST narrow band photometry, and the Be phenomenon actually more widespread. Secondly, a narrow absorption feature is observed at the center of the reversed core of the $H\delta$ line for target 83. This feature could be the result of absorption from the decretion disk if the star is seen at a large inclination angle, as described for $H\alpha$ lines in shell stars (e.g., Rivinius et al. 2013; Sigut & Ghafourian 2023). This contrasts with the shell parameter of target 83, however, estimated to 1.2, which suggests an inclination lower than 70° (Sigut & Ghafourian 2023). From MIKE data, absorption features for target 83 are observed at the center of the $H\alpha$, $H\beta$, $H\gamma$ and $H\delta$, which further supports absorption from the decretion disk (see Fig. B3). Those results suggest that the inclination of some of the stars is difficult to estimate from shell parameters. Additional high resolution spectra recorded with, e.g., MIKE targeting $H\alpha$, $H\beta$, $H\gamma$ and $H\delta$, along with accurate modeling of the emission lines in Be stars (see, e.g., Sigut & Ghafourian 2023), would allow us to provide better constraints on the inclination angle of the observed targets, and to accurately classify the narrow $H\alpha$ emitters identified in this work.

With both M2FS and MIKE spectra, $H\alpha$ nebular emission was observed. The nebular emission is successfully corrected by the MIKE reduction pipeline, extracting the sky and science spectra from a single aperture, but is impossible to accurately correct for observations collected with M2FS with the setup currently used. The narrow width of the nebular emission (of a few dozens of pixels only) is unlikely to significantly impact the results of photometric studies observing the broad and strong $H\alpha$ emission of bright targets. However, its contribution is more significant for the measurements of faint stars, in particular if they are slowly rotating and have narrower stellar $H\alpha$ features suggesting that Be stars may be more frequent than presently thought. Future observations in clusters with nebular emission envisioned with fiber systems should attempt to measure spectra on sky in regions immediately adjacent to the targets positions in order to provide a better correction of those features. We find no B star close to the cluster core (see Fig. 3). Although our selection criteria for M2FS introduce a bias towards choosing isolated targets outside of the crowded cluster core, this is in line with the previous results (Bodensteiner et al. 2020) suggesting that the ratio of Be stars in the core is higher than in the outskirts of the cluster. Those results are also consistent with the number of B and Be stars estimated from HST photometry inside and outside of the cluster core (see Fig. 10). The narrow $H\alpha$ emitters were detected outside of the cluster core, however, which could indicate that the number of Be stars in the outskirts of the cluster is also underestimated. It should be noted that the bias towards bright targets is likely to lead to higher Be detection rates in our sample than in other studies, given the larger overall content in Be stars in the photometric data published by Milone et al. (2018) for brighter tar-

gets. Further high-resolution spectroscopic observations of NGC 330 will help to better characterize the observed stars by allowing us to probe the the core of the emission lines which is necessary to better constrain the properties of the targets, and better understand the multiple populations observed in the CMD. In particular, future observations carried out with high resolution spectrographs could be used to search for features indicative of binary systems.

This research has made use of NASA’s Astrophysics Data System Bibliographic Services and of the data products from 2MASS, which is a joint project of the University of Massachusetts and IPAC/Caltech, funded by NASA and the NSF.

This work has made use of the VALD database, operated at Uppsala University, the Institute of Astronomy RAS in Moscow, and the University of Vienna.

This work has received funding from “PRIN 2022 2022MMEB9W - *Understanding the formation of globular clusters with their multiple stellar generations*” (PI Anna F. Marino).

We thank Christian Johnson for preparing the fibre configurations for M2FS observations and Morgan MacLeod for fruitful discussions regarding the content of this paper. We thank Aaron Sigut for discussions regarding the modeling of line profiles.

Facility: Magellan: Clay (M2FS, MIKE).

Software: Astropy (Astropy Collaboration et al. 2013a, 2018, 2022) / ccdproc (Astropy Collaboration et al. 2013b; Craig et al. 2017), CarPy (Kelson et al. 2000; Kelson 2003), Numba (Lam et al. 2015).

APPENDIX

A. BEST FITS TO THE DATA

For the targets studied in this paper, Fig. A1 presents the spectra recorded with M2FS in 2022, and Fig. A2 presents the spectra recorded with MIKE in 2021. On each figure, we show the best fit of the TLUSTY model to the He I and $H\delta$ lines.

Fig. Set A1. $H\delta$, He I line at 4143.76 Å and $H\alpha$ line profiles observed with M2FS in 2022.

Fig. Set A2. Hydrogen, Helium and Carbon lines identified in MIKE spectra.

B. HYDROGEN LINES FROM MIKE DATA

Figure B3 shows the $H\alpha$, $H\beta$, $H\gamma$, $H\delta$ and the He I line at 4143.7Å for 5 targets observed with MIKE.

Fig. Set B3. $H\alpha$, $H\beta$, $H\gamma$, $H\delta$ line profiles from MIKE spectra

REFERENCES

- Astropy Collaboration, Robitaille, T. P., Tollerud, E. J., et al. 2013a, A&A, 558, A33, doi: 10.1051/0004-6361/201322068
- . 2013b, A&A, 558, A33, doi: 10.1051/0004-6361/201322068

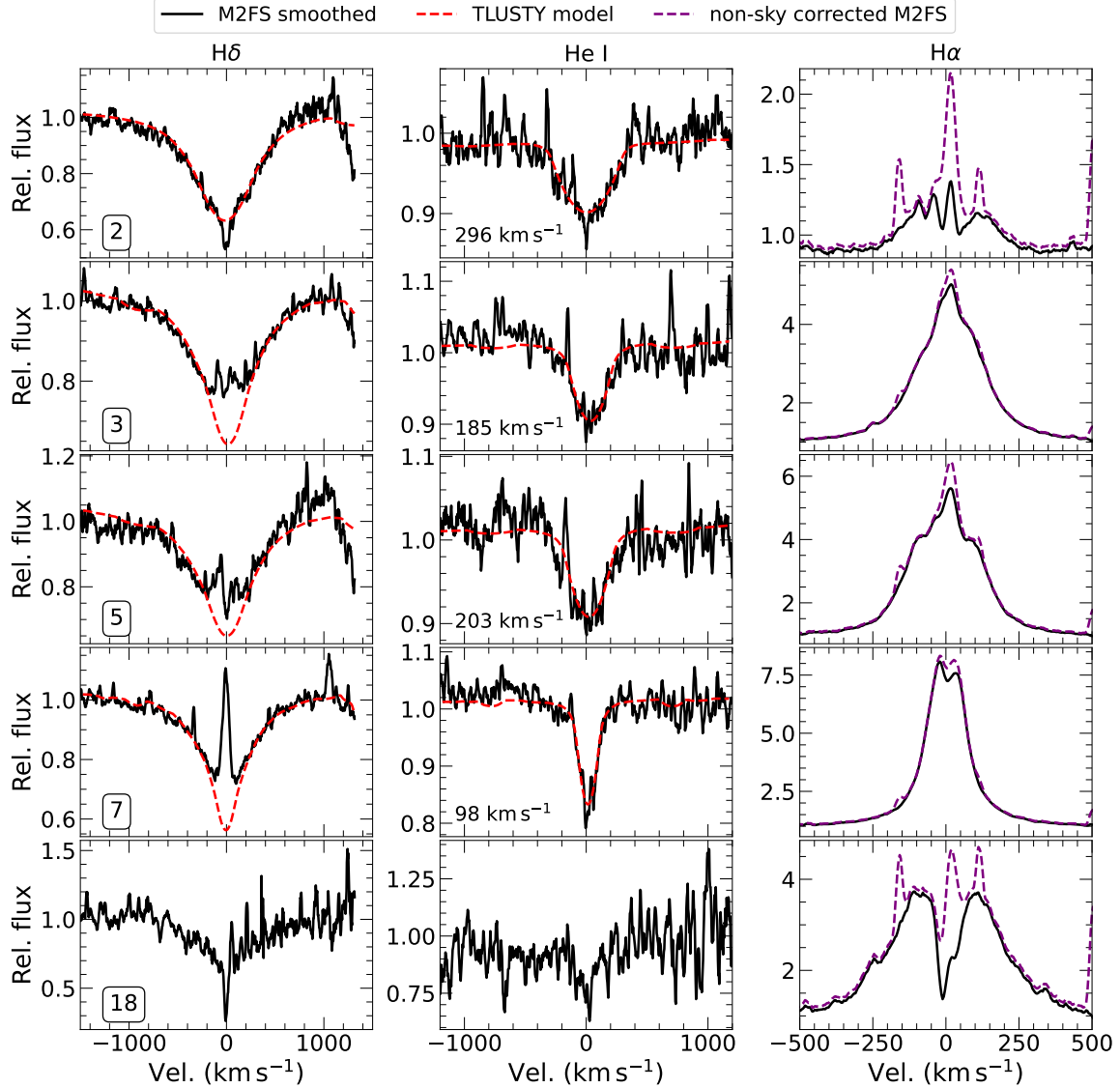


Figure A1. $H\delta$, He I line at 4143.76 \AA and $H\alpha$ line profiles observed with M2FS in 2022 for 5 targets in NGC 330. The $H\alpha$ line is presented before and after sky correction. The best obtained fit of TLUSTY models to the $H\delta$ and He I lines are shown in dashed red, when available. Projected rotational velocity estimated from the fits are indicated when available.

Astropy Collaboration, Price-Whelan, A. M., Sipőcz, B. M., et al. 2018, *AJ*, 156, 123, doi: [10.3847/1538-3881/aabc4f](https://doi.org/10.3847/1538-3881/aabc4f)

Astropy Collaboration, Price-Whelan, A. M., Lim, P. L., et al. 2022, *ApJ*, 935, 167, doi: [10.3847/1538-4357/ac7c74](https://doi.org/10.3847/1538-4357/ac7c74)

Bastian, N., & de Mink, S. E. 2009, *MNRAS*, 398, L11, doi: [10.1111/j.1745-3933.2009.00696.x](https://doi.org/10.1111/j.1745-3933.2009.00696.x)

Bastian, N., & Lardo, C. 2018, *ARA&A*, 56, 83, doi: [10.1146/annurev-astro-081817-051839](https://doi.org/10.1146/annurev-astro-081817-051839)

Bastian, N., Cabrera-Ziri, I., Niederhofer, F., et al. 2017, *MNRAS*, 465, 4795, doi: [10.1093/mnras/stw3042](https://doi.org/10.1093/mnras/stw3042)

Bernstein, R., Shtetman, S. A., Gunnels, S. M., Mochnacki, S., & Athey, A. E. 2003, in *Society of Photo-Optical Instrumentation Engineers (SPIE) Conference Series*, Vol. 4841, Instrument Design and Performance for Optical/Infrared Ground-based Telescopes, ed. M. Iye & A. F. M. Moorwood, 1694–1704, doi: [10.1117/12.461502](https://doi.org/10.1117/12.461502)

Bodensteiner, J., Sana, H., Mahy, L., et al. 2020, *A&A*, 634, A51, doi: [10.1051/0004-6361/201936743](https://doi.org/10.1051/0004-6361/201936743)

Bodensteiner, J., Sana, H., Wang, C., et al. 2021, *A&A*, 652, A70, doi: [10.1051/0004-6361/202140507](https://doi.org/10.1051/0004-6361/202140507)

Bodensteiner, J., Sana, H., Dufton, P. L., et al. 2023, *A&A*, 680, A32, doi: [10.1051/0004-6361/202345950](https://doi.org/10.1051/0004-6361/202345950)

Choi, J., Dotter, A., Conroy, C., et al. 2016, *ApJ*, 823, 102, doi: [10.3847/0004-637X/823/2/102](https://doi.org/10.3847/0004-637X/823/2/102)

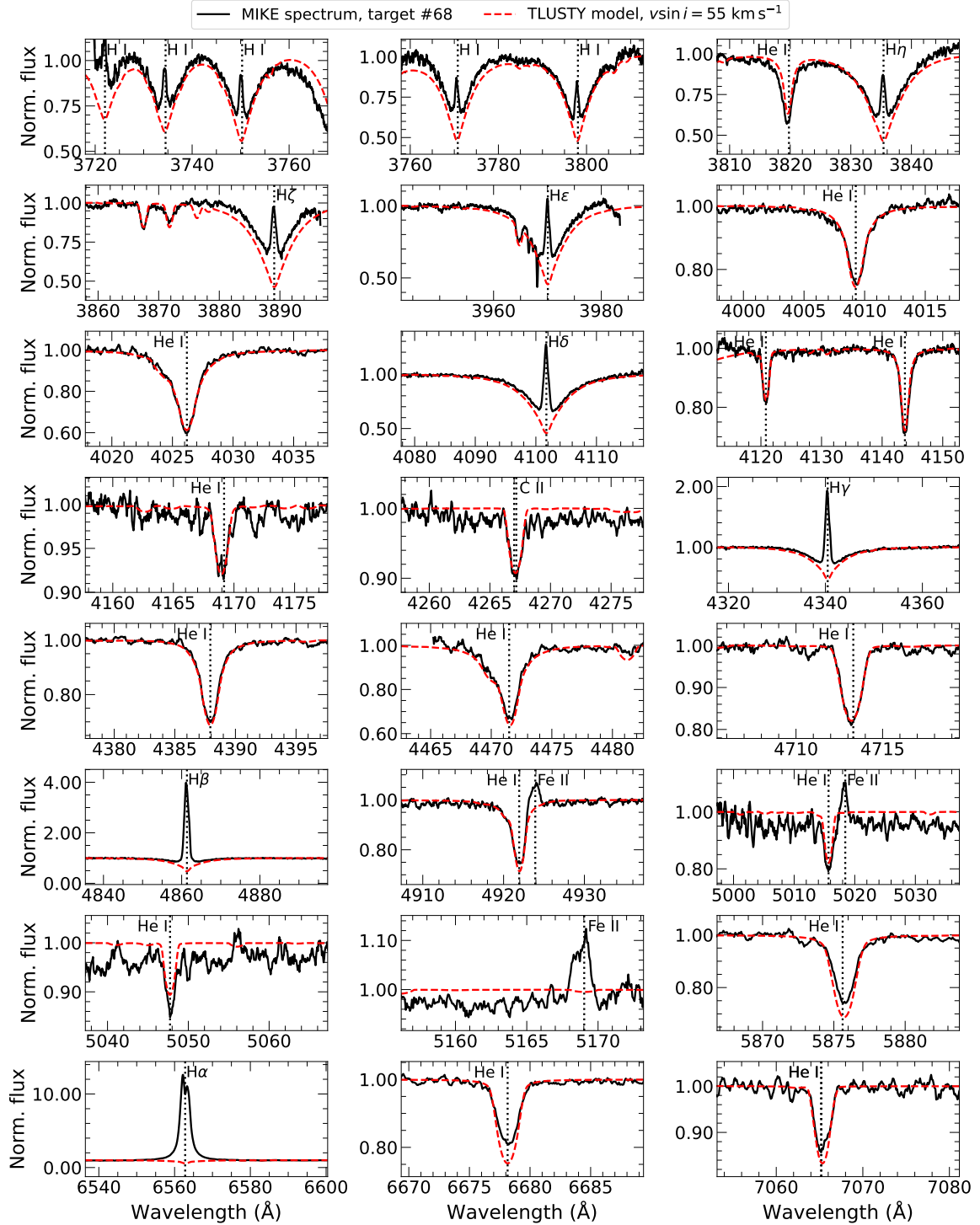


Figure A2. Hydrogen, helium, carbon and iron lines identified in the MIKE spectrum of target 68. The best fit of TLUSTY models is shown in dashed red.

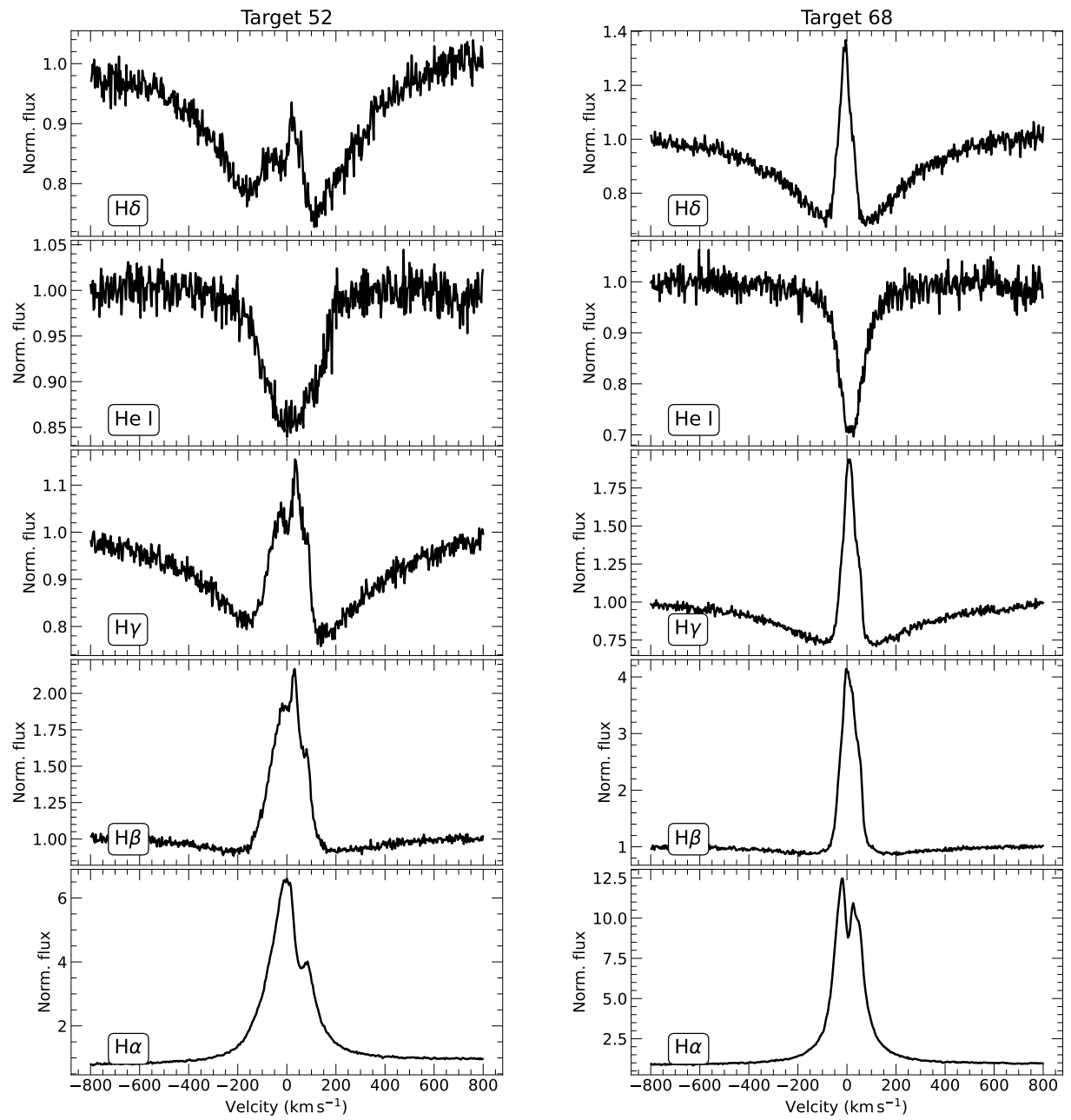


Figure B3. MIKE data for targets 52 and 68, showing the profile of the $H\alpha$, $H\beta$, $H\gamma$, $H\delta$, and the He I line at 4143.76 \AA

- Conroy, C., & Spergel, D. N. 2011, *ApJ*, 726, 36, doi: [10.1088/0004-637X/726/1/36](https://doi.org/10.1088/0004-637X/726/1/36)
- Correnti, M., Goudfrooij, P., Bellini, A., Kalirai, J. S., & Puzia, T. H. 2017, *MNRAS*, 467, 3628, doi: [10.1093/mnras/stx010](https://doi.org/10.1093/mnras/stx010)
- Craig, M., Crawford, S., Seifert, M., et al. 2017, *Astropy/Ccdproc: V1.3.0.Post1, v1.3.0.post1*, Zenodo, Zenodo, doi: [10.5281/zenodo.1069648](https://doi.org/10.5281/zenodo.1069648)
- Cristofari, P. I., & Walker, M. G. 2024, *M2FS-RS: Data reduction pipeline for M2FS, 0.0.1*, Zenodo, doi: [10.5281/zenodo.11479585](https://doi.org/10.5281/zenodo.11479585)
- D'Antona, F., Di Criscienzo, M., Decressin, T., et al. 2015, *MNRAS*, 453, 2637, doi: [10.1093/mnras/stv1794](https://doi.org/10.1093/mnras/stv1794)
- D'Antona, F., Milone, A. P., Tailo, M., et al. 2017, *Nature Astronomy*, 1, 0186, doi: [10.1038/s41550-017-0186](https://doi.org/10.1038/s41550-017-0186)
- Dotter, A. 2016, *ApJS*, 222, 8, doi: [10.3847/0067-0049/222/1/8](https://doi.org/10.3847/0067-0049/222/1/8)
- Dupree, A. K., Dotter, A., Johnson, C. I., et al. 2017, *ApJL*, 846, L1, doi: [10.3847/2041-8213/aa85dd](https://doi.org/10.3847/2041-8213/aa85dd)
- Eldridge, J. J., Beasor, E. R., & Britavskiy, N. 2020, *MNRAS*, 495, L102, doi: [10.1093/mnrasl/slaa067](https://doi.org/10.1093/mnrasl/slaa067)
- Goudfrooij, P., Girardi, L., Kozhurina-Platais, V., et al. 2014, *ApJ*, 797, 35, doi: [10.1088/0004-637X/797/1/35](https://doi.org/10.1088/0004-637X/797/1/35)
- Hanuschik, R. W. 1996, *A&A*, 308, 170
- Hubeny, I., & Lanz, T. 1995, *ApJ*, 439, 875, doi: [10.1086/175226](https://doi.org/10.1086/175226)
- Iqbal, S., & Keller, S. C. 2013, *MNRAS*, 435, 3103, doi: [10.1093/mnras/stt1502](https://doi.org/10.1093/mnras/stt1502)
- Keller, S. C., Bessell, M. S., & Da Costa, G. S. 2000, *AJ*, 119, 1748, doi: [10.1086/301282](https://doi.org/10.1086/301282)
- Keller, S. C., Mackey, A. D., & Da Costa, G. S. 2011, *ApJ*, 731, 22, doi: [10.1088/0004-637X/731/1/22](https://doi.org/10.1088/0004-637X/731/1/22)
- Kelson, D. D. 2003, *PASP*, 115, 688, doi: [10.1086/375502](https://doi.org/10.1086/375502)
- Kelson, D. D., Illingworth, G. D., van Dokkum, P. G., & Franx, M. 2000, *ApJ*, 531, 159, doi: [10.1086/308445](https://doi.org/10.1086/308445)
- Klement, R., Carciofi, A. C., Rivinius, T., et al. 2017, *A&A*, 601, A74, doi: [10.1051/0004-6361/201629932](https://doi.org/10.1051/0004-6361/201629932)
- Kramida, A., Yu. Ralchenko, Reader, J., & and NIST ASD Team. 2023, *NIST Atomic Spectra Database (ver. 5.11)*, *NIST Atomic Spectra Database (ver. 5.11)*, [Online]. Available: <https://physics.nist.gov/asd> [2017, April 9]. National Institute of Standards and Technology, Gaithersburg, MD.
- Lam, S. K., Pitrou, A., & Seibert, S. 2015, in *Proc. Second Workshop on the LLVM Compiler Infrastructure in HPC*, 1–6, doi: [10.1145/2833157.2833162](https://doi.org/10.1145/2833157.2833162)
- Lanz, T., & Hubeny, I. 2007, *ApJS*, 169, 83, doi: [10.1086/511270](https://doi.org/10.1086/511270)
- Mackey, A. D., Broby Nielsen, P., Ferguson, A. M. N., & Richardson, J. C. 2008, *ApJL*, 681, L17, doi: [10.1086/590343](https://doi.org/10.1086/590343)
- Mateo, M., Bailey, J. I., Crane, J., et al. 2012, in *Society of Photo-Optical Instrumentation Engineers (SPIE) Conference Series*, Vol. 8446, *Ground-based and Airborne Instrumentation for Astronomy IV*, ed. I. S. McLean, S. K. Ramsay, & H. Takami, 84464Y, doi: [10.1117/12.926448](https://doi.org/10.1117/12.926448)
- Milone, A. P., Bedin, L. R., Cassisi, S., et al. 2013, *A&A*, 555, A143, doi: [10.1051/0004-6361/201220567](https://doi.org/10.1051/0004-6361/201220567)
- Milone, A. P., Bedin, L. R., Piotto, G., & Anderson, J. 2009, *A&A*, 497, 755, doi: [10.1051/0004-6361/200810870](https://doi.org/10.1051/0004-6361/200810870)
- Milone, A. P., Marino, A. F., D'Antona, F., et al. 2016, *MNRAS*, 458, 4368, doi: [10.1093/mnras/stw608](https://doi.org/10.1093/mnras/stw608)
- . 2017, *MNRAS*, 465, 4363, doi: [10.1093/mnras/stw2965](https://doi.org/10.1093/mnras/stw2965)
- Milone, A. P., Marino, A. F., Di Criscienzo, M., et al. 2018, *MNRAS*, 477, 2640, doi: [10.1093/mnras/sty661](https://doi.org/10.1093/mnras/sty661)
- Okazaki, A. T. 1991, *PASJ*, 43, 75
- . 1997, *A&A*, 318, 548
- Papaloizou, J. C. B., & Savonije, G. J. 2006, *A&A*, 456, 1097, doi: [10.1051/0004-6361:20065407](https://doi.org/10.1051/0004-6361:20065407)
- Patrick, L. R., Lennon, D. J., Evans, C. J., et al. 2020, *A&A*, 635, A29, doi: [10.1051/0004-6361/201936741](https://doi.org/10.1051/0004-6361/201936741)
- Paxton, B., Bildsten, L., Dotter, A., et al. 2011, *ApJS*, 192, 3, doi: [10.1088/0067-0049/192/1/3](https://doi.org/10.1088/0067-0049/192/1/3)
- Paxton, B., Cantiello, M., Arras, P., et al. 2013, *ApJS*, 208, 4, doi: [10.1088/0067-0049/208/1/4](https://doi.org/10.1088/0067-0049/208/1/4)
- Paxton, B., Marchant, P., Schwab, J., et al. 2015, *ApJS*, 220, 15, doi: [10.1088/0067-0049/220/1/15](https://doi.org/10.1088/0067-0049/220/1/15)
- Piatti, A. E., Pietrzyński, G., Narloch, W., Górski, M., & Graczyk, D. 2019, *MNRAS*, 483, 4766, doi: [10.1093/mnras/sty3473](https://doi.org/10.1093/mnras/sty3473)
- Rivinius, T., Carciofi, A. C., & Martayan, C. 2013, *A&A Rv*, 21, 69, doi: [10.1007/s00159-013-0069-0](https://doi.org/10.1007/s00159-013-0069-0)
- Sigut, T. A. A., & Ghafourian, N. R. 2023, *ApJ*, 948, 34, doi: [10.3847/1538-4357/ac940c](https://doi.org/10.3847/1538-4357/ac940c)
- Vinicius, M. M. F., Zorec, J., Leister, N. V., & Levenhagen, R. S. 2006, *A&A*, 446, 643, doi: [10.1051/0004-6361:20053029](https://doi.org/10.1051/0004-6361:20053029)
- Walker, M. G., Caldwell, N., Mateo, M., et al. 2023, *ApJS*, 268, 19, doi: [10.3847/1538-4365/acdd79](https://doi.org/10.3847/1538-4365/acdd79)
- Wisniewski, J. P., & Bjorkman, K. S. 2006, *ApJ*, 652, 458, doi: [10.1086/507260](https://doi.org/10.1086/507260)
- Zorec, J., Hubert, A. M., Martayan, C., & Frémat, Y. 2023, *A&A*, 676, A81, doi: [10.1051/0004-6361/202346018](https://doi.org/10.1051/0004-6361/202346018)